Journal Name

ROYAL SOCIETY OF CHEMISTRY

ARTICLE

MoS₂ nanosheets with expanded interlayer spacing for enhanced sodium storage

Huishuang Dong,[a] Yang Xu,*[b] Chenglin Zhang,[b] Yuhan Wu,[b] Min Zhou,[b] Long Liu,[b] Yulian Dong,[a] Qun Fu,[a] Minghong Wu [a] and Yong Lei *[a,b]

Sodium-ion battery technology is a promising alternative to lithium-ion batteries for low-cost and large-scale energy storage applications. The larger size of Na-ion relative to Li-ion imposes kinetic limitation and often results in sluggish Na-ion diffusion. It is a great necessity to explore prominent structural features of materials to overcome the limitation and improve the diffusion. Layered MoS₂ has an ideal two-dimensional diffusion pathways because of the weak van der Waals interaction between the layers. However, the limited gallery height of 0.3 nm is insufficient to achieve fast Na-ion diffusion. A facile hydrothermal route at medium-ranged temperatures is reported in this work to obtain interlayer expanded MoS₂ naonsheets. The interlayer spacing is greatly expanded to 1 nm and facilitates Na-ion insertion and extraction in the van der Waal gaps. The nanosheet morphology shortens Na-ion diffusion distance from the lateral side. The interlayer expanded MoS₂ nanosheets are used as sodium-ion battery anodes in the voltage window of 0.5-2.8 V where intercalation reaction contributes to Na-storage and the layered structure can be preserved. The nanosheets exhibit a high cycling stability by retaining 92% of the initial charge capacity after 100 cycles and a great rate capability 43 mAh g⁻¹ at 2 A g⁻¹. Kinetics study reveals a significant alleviation of diffusional limitation, verifying the improved Na-ion diffusion and enhanced Na-storage. The presented work explores the utilization of the van der Waals gaps to store ions and sheds light on designing two-dimensional materials in other energy systems.

1. Introduction

Two-dimensional (2D) nanomaterials have gained world-wide attention for energy storage and conversion applications owing to their fascinating structural features, i.e., the ultra-thinness of atomic layers and the 2D channels between the layers.[1-6] As a representative, 2D transition metal dichalcogenides (TMDs) have been widely applied in many energy related research domains.[7-9] TMDs possess a unique lamellar structure characterized by the hexagonally coordinated chalcogen-metal-chalcogen (C-M-C) layers and the van der Waals force between the layers. The weak van der Waals force allows the intercalation of ions between the layers without significant structural distortion. This characteristic makes the interlayer space ideal 2D ion diffusion pathways, as an importance feature for a material to be used in batteries.

Molybdenum disulfide MoS₂ is a typical 2D TMD and has been heavily studied in lithium- and sodium-ion batteries (LIBs and SIBs) so far.[10,11] However, the larger size of Na-ion (1.02 Å)

relative to Li-ion (0.76 Å) has imposed a major challenge for Na-ion intercalation/diffusion in the van der Waals gaps. Recent theoretical simulations and experimental observations have shown that a minimum interlayer spacing of 0.37 nm is required for Na-ion intercalation, and this spacing is much larger than that required for Li-ion intercalation (0.34 nm).[12,13] Multi-layered MoS₂ nanosheets generally exhibit an interlayer spacing of ~0.62 nm, which leads to a gallery height of ~0.30 nm between two adjacent layers by taking the size of Mo and S atoms into consideration.[14,15] The narrow gallery height restricts the kinetics of Li-ion diffusion and is even more critical for Na-ion diffusion since its size is 34% larger. Therefore, the restriction calls for strategies that can improve the kinetics of Na-ion diffusion in MoS₂.

Expanding interlayer spacing is a straightforward strategy to increase the gallery height, which could directly alleviate the above-mentioned restriction. Two criteria need to be met to ensure the proper functioning of expanded interlayer spacing. First criterion is that a substantial expansion is necessary, for which a dilemma has be to overcome. In some previous works, the expansion is very limited, typically being less than 0.7 nm.[16-18] Some other works reported a large expansion to about 1 nm, but large-sized guest species need to be intercalated between the layers during the synthesis, such as carbons,[19,20] polyaniline,[21] polyvinylpyrrolidone,[22] ethylenedianime,[23] and glucose.[23] Such pre-intercalation usually requires high temperature and tedious fabrication steps as well as sometimes careful post-treatments to ensure the deintercalation of the

guest species. In some cases, incomplete deintercalation may result in less accessible interlayer space to accommodate Na-ions. It is of great importance to develop a facile synthetic route to obtain substantial expansion of interlayer spacing in MoS_2. Second criterion is that a proper voltage window is required to ensure the preservation of the layered structure. It has become a popular motive that most of previous works were in pursue of high capacity derived from the four-electron conversion reaction of MoS_2. This could inevitably restack or aggregate the MoS_2 layers and destroy the van der Waals gaps as 2D diffusion pathways, which is evidenced by the detection of Mo and sulfide phases during cycling process,[24,25] leaving the integrity of the interlayer expansion questionable. It is thus critical to control the voltage window in which an intercalation reaction, rather than a conversion reaction, dominates Na-ion storage.

Herein, we report in this work MoS_2 nanosheets as SIB anodes by meeting both above discussed criteria. A facile hydrothermal route is developed to synthesize MoS_2 nanosheets at medium-ranged temperatures. The nanosheets exhibit a substantially expanded interlayer spacing of 1 nm and are tested as anodes in a voltage range of 0.5-2.8 V (vs. Na^+/Na) where an intercalation reaction takes place to store Na-ions. The nanosheets synthesized at 140°C deliver a high initial charge capacity of 195 mAh g^{-1} at 50 mA g^{-1}, while those synthesized at 160°C show a high cycling stability by retaining 92% of the initial charge capacity after 100 cycles and a great rate capability 43 mAh g^{-1} at 2 A g^{-1}. Both the low rate capacity and rate capability are among the best results of Na-storage in the applied voltage window. We believe our work might shed light on the interlayer engineering of 2D TMDs and provide a material platform and insights for a wide range of energy related applications.

2. Experimental section

2.1 Synthesis of MoS_2 nanosheets with an expanded interlayer spacing

MoS_2 nanosheets with an expanded interlayer spacing were synthesized by a hydrothermal method. In a typical procedure, 1 mmol $(NH_4)_6Mo_7O_{24}\cdot4H_2O$ and 30 mmol thiourea were dissolved in 35 ml DI water under stirring. The solution was kept stirring for 0.5 h, and then the obtained transparent solution was transferred to a Teflon-lined stainless-steel autoclave. The autoclave was sealed and maintained at 140°C or 160°C for 24 h. After cooling to room temperature naturally, the powders were collected by centrifuging the mixture, rinsed with absolute ethanol several times, and then dried in vacuum at 60°C.

2.2 Material characterizations

Characterizations of the nanosheets were carried out by X-ray diffractometry (D/MAX2500V PC diffractometer, Cu Kα λ = 1.54 Å), Raman spectroscopy (inVia Raman microscope), X-ray photoelectron spectroscopy (Thermo SCIENTIFIC ESCALAB 250Xi), scanning electron microscopy (Zeiss AURIGA@), and transmission electron microscopy (JEOL JEM-2100F).

2.3 Electrochemical measurements

Electrodes were fabricated by mixing the nanosheets, Super P and poly(vinylidenedifluoride) (PVDF) with a weight ratio of 7:2:1. The mixture was coated uniformly (doctor-blade) on a copper foil with a mass loading of 1-2 mg cm^{-2}, and then dried at 110°C under vacuum for more than 12 h. Electrochemical measurements were carried out using coin cells, CR2032 and the cells were assembled in a nitrogen-filled glovebox with oxygen and moisture concentrations being kept below 0.1 ppm. Na foil used as counter electrode was separated from working electrode by a layer of glass microfiber filter (Whatman, Grade GF/B). Electrolyte was 1 M sodium perchlorate ($NaClO_4$) in an ethylene carbonate (EC)/diethyl carbonate (DEC) solution (1:1). Cyclic voltammetry and EIS was performed on a VSP electrochemical workstation (Bio-Logic, France) in a scan rate range of 0.1-2 mV s^{-1}. Galvanostatic charge/discharge was performed on a Land CT 2001A battery testing system (Land, China) at current densities of 0.05-2 A g^{-1} at room temperature.

3. Results and discussion

3.1 Characterizations

MoS_2 with an expanded interlayer spacing were obtained by reacting ammonium molybdate and thiourea in an excess stoichiometric ratio (1:30). For simplification, samples obtained at 140 and 160°C are labelled as E140 and E160, respectively. Fig. 1a shows the X-ray diffraction (XRD) patterns of the samples and the standard pattern of MoS_2 (JCPDS 37-1492). A significant shift of (002) peak from 14.4° to 8.9° can been seen. It indicates the interlayer spacing has been substantially expanded from 0.63 nm in the standard pattern to around 1.0 nm in the as-obtained samples. A new peak appearing at 17.8° corresponds to the (004) diffraction and provides an additional support for the expanded interlayer spacing.[26,27] Two broadened peaks centred at 32° and 57° can be indexed to (100) and (110) planes, respectively, suggesting the same atomic orientation of the samples along the basal plane. It is worth noting that E160 shows less broadened peaks and higher peak intensity than E140, which indicates higher crystallinity and less disordered structure of E160. These features could contribute to a better cycling stability, as will be discussed later. Fig. 1b shows the Raman spectra of the samples. Three strong peaks located at 283, 376 and 405 cm^{-1} are assigned to the 2H-MoS_2 vibration modes of E_{1g}, E^1_{2g} (in-plane) and A_{1g} (out-of-plane), respectively. Another three peaks that are characteristic of the 1T-MoS_2 phase can also be seen at 149, 237 and 335 cm^{-1}, being ascribed to J1, J2 and J3 mode, respectively.[28,29] It has been previously reported that a phase transition from 2H to 1T occurs when expanding the interlayer spacing of MoS_2,[19,30] which could account for our observations. The coexistence of 2H and 1T phase can be further verified by the X-ray photoelectron spectroscopy (XPS) measurement. Fig. 1c shows the Mo 3d core-level spectra of the two samples. The peaks at 229.0 and 232.4 eV can be assigned to the Mo $3d_{5/2}$ and $3d_{3/2}$ of 2H-MoS_2, respectively. Another two peaks at 228.2 and 231.6 eV with the lower binding energies by ~0.8 eV are attributed to the existence of 1T-MoS_2.[28,31] Fig. 1d shows the S 2p core-level

spectra, where both 2H and 1T phases can be observed from the shifting of the peaks to a lower binding energy. According to the relative peak intensity of the 2H and 1T phase, E160 has a lower content of 1T phase comparing with E140, suggesting temperature is a critical factor to control the phase composition. Therefore, phase characterization reveals not only the substantial expansion of the interlayer spacing but also the coexistence of 1T and 2H phase in both samples.
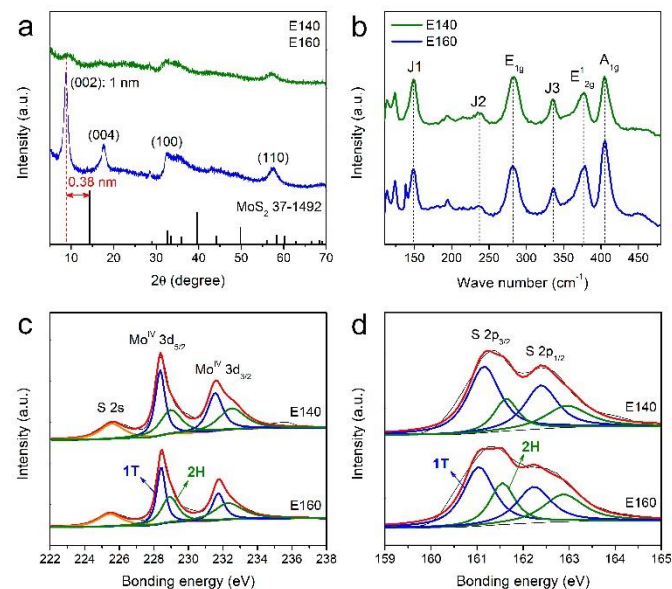

Fig. 1 Phase characterization of E140 and E160. (a) XRD patterns. (b) Raman spectra. (c) Mo 3d XPS spectra. (d) S 2p XPS spectra.

The morphology of the as-obtained samples was examined by field emission scanning electron microscopy (FESEM). Fig. 2a and 2c outline both samples have a morphology of nanosheet with a uniform lateral size in the range of 150-200 nm. The nanosheets loosely interconnect with each other and form flower-like architectures. High-magnification images in Fig. 2b and 2d illustrate the rippled edges of the nanosheets. More corrugations along the edge of the nanosheets can be observed in E140 than E160, giving a slightly larger thickness of the former (10-12 nm) than the latter (9-10 nm). We speculate that the insufficient crystallization caused by a lower synthesis temperature could result in a more disordered microstructure, which is visually reflected by the more ripped edges of the nanosheets. Nevertheless, both samples show a high yield of the nanosheet morphology and an ultrathin characteristic that is stacked by about ten molecular layers according to the interlayer spacing calculated in the XRD patterns. Surface area and porous texture of the samples were analyzed using N_2-adsorption. As shown in Fig. 2e and 2f, both samples exhibit type IV isotherms with hype H3 hysteresis loops, showing a meso/macroporous structure. The Brunauer-Emmett-Teller (BET) surface area was calculated to be 21.69 and 19.91 $m^2 g^{-1}$ for E140 and E160, respectively. Both samples display two peaks in pore size distribution. Pores that are smaller than 3 nm are ascribed to the crystallographic defects, and those that are around 30 nm are generated by the space between the nanosheets. The samples exhibit similar surface area and

porous texture, suggesting a minimal effect on the performance difference between E140 and E160.
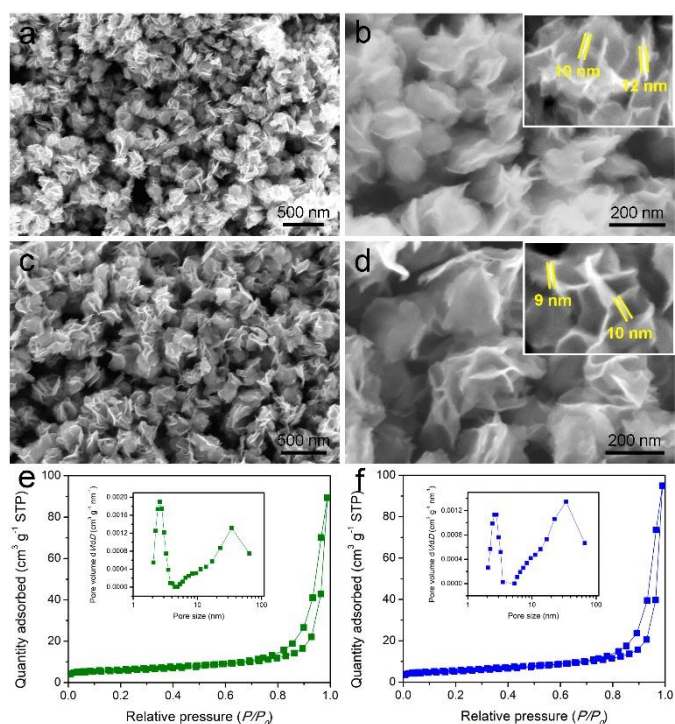

Fig. 2 Morphology characterization of E140 (a and b) and E160 (c and d). (a and c) Low-magnification SEM images. (b and d) High-magnification SEM images. Nitrogen adsorption-desorption isotherms (inset: pore size distribution) of E140 (e) and E160 (f).

The microstructure of the as-obtained samples was characterized by transmission electron microscopy (TEM). As shown in Fig. 3a and 3b, the flower-like architectures can be observed and the lateral size of the nanosheets is estimated to be 150-200 nm, being agreement with the SEM results. High-resolution TEM (HRTEM) images give direct depiction of the side and basal planes of the nanosheets. Fig. 3c and 3d show a typical lamellar structure with an interlayer spacing estimated to be around 1 nm, which is in accordance with the XRD results. The crystal fringes of the nanosheets are discontinuous along the crippled edges, for which a higher discontinuity can be observed in E140, leading to a larger thickness comparing with E160. The observed discontinuity in E140 also implies a higher content of crystallographic defects.[32,33] It can be confirmed by the HRTEM images of the basal planes. As shown in Fig. 3e and 3f, a lattice fringe of 0.27 nm, corresponding to the spacing of (001) plane, can be seen in both samples, once again demonstrating the same atomic orientation along this dimension. However, the lattice fringes are not consistent over the entire basal surface and slightly rotate from one micro-region to another. It is worth noting that comparing with E140, E160 shows clearer lattice fringes with a lower degree of distortion and thus has less defects in the basal plane, which corresponds to its more continuous fringes in the side view (Fig. 3d). The less defects in E160 also induce less nano-domains in the basal plane, which is evidenced by the less broadened (100) and (110) peaks in Fig.

1a. To summarize the phase, morphology and microstructure characterizations, the as-obtained MoS$_2$ nanosheets possess an expanded interlayer spacing of 1 nm and a mixed phase of 2H and 1T. E160 shows higher crystallinity and less defects than E140, which is expected to provide a better structural stability upon Na-ion intercalation and de-intercalation.
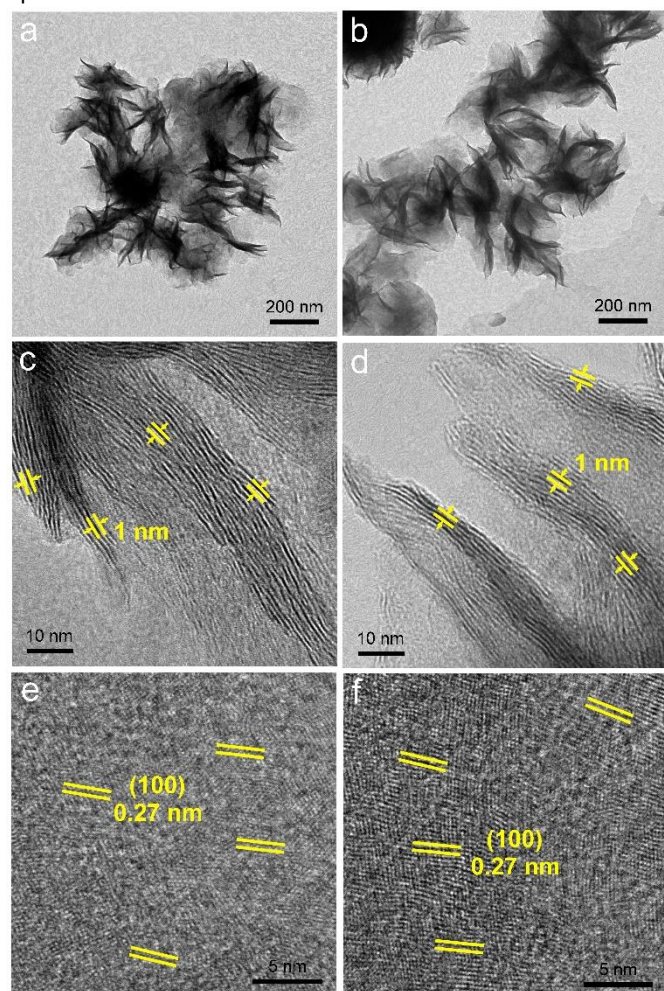

Fig. 3 Microstructure characterization of E140 (a, c and e) and E160 (b, d and f). (a and b) TEM images. (c-f) HRTEM images.

3.2 Sodium storage performance

Na-storage behaviour of the samples was tested using cyclic voltammetry (CV) and galvanostatic charge/discharge measurement. The voltage range was set to be 0.5-2.8 V (vs. Na$^+$/Na) to ensure no crystal reconstruction derived from the conversion reaction occurs upon Na-ion (de)intercalation. Previous studies showed that Na intercalation in MoS$_2$ occurs at a voltage above 0.4 V, beyond which conversion reaction takes place and the layered structure collapses.[34,35] Fig. S1 in the ESI† shows the CV curves of the first three cycles at a scan rate of 0.1 mV s^{-1}. For the case of E140 (Fig. S1a in the ESI†), it exhibits no well-defined redox peaks in cycle1. Several humps appearing at 1.86, 1.54, 1.41, 1.20 and 0.80 V as well as a slope extending to the cut-off voltage can be seen in the cathodic scan, while the corresponding humps at 1.60, 1.84, 2.16, 2.54 and 2.69 V can be seen in the subsequent anodic scan. For the case of E160 (Fig.

S1b in the ESI†), it exhibits less contoured humps, resulting in a pair of much widened peaks centred at 1.30/1.52 V and a slope extending to the cut-off voltage. Similar curves are seen in cycle2 and 3, showing no apparent peaks. The curves of E160 display a better overlapping shape than those of E140, indicating a better cycling stability. The observed CV curves are very different from those of bulk MoS$_2$ with a much smaller interlayer spacing, where it exhibits two well defined cathodic peaks (0.8-0.9 V and 0.7-0.8 V) that correspond to a two-staged intercalation of Na-ion.[35,36] The interlayer spacing presented here is expanded to 1 nm, which largely opens up the van der Waal gaps and minimizes the Na-intercalation energy. The disordered structure derived from the low crystallinity may provide more intercalation sites and thus deliver a wide range of intercalation voltage.[37] Fig. 4a and 4b show the charge/discharge profiles of the first three cycles at a current density of 50 mA g^{-1}. E140 displays no well-defined plateaus while E160 displays smoother profiles than E140, both of which are consistent with the CV observations. E140 delivers cycle1 charge and discharge capacity of 195 and 275 mAh g^{-1}, respectively, as well as a cycle1 Columbic Efficiency (CE) of 71%. The corresponding values of E160 are 119 and 206 mAh g^{-1} as well as 58%. It has been previously reported that amorphous materials or materials with low crystallinity could have a more open framework that can form percolation pathways via the opening of active diffusion channels and facilitate Na-ion diffusion owing to the quasi-isotropic characteristic.[38-40] We therefore attribute the higher capacities of E140 to its more disordered structure that provides more Na-ion intercalation sites and less Na-ion diffusion resistance comparing with E160. The higher initial CE of E140 could be ascribed to the more open framework and more Na-ion (de)intercalation sites, which could reduce the distance for Na-ions to diffuse in and out of the interlayer space, thus reducing the trapping of Na-ions in the interlayer space. Similar phenomenon was previously observed in amorphous SnO$_2$.[41] Despite the lower initial capacities, E160 exhibits a better cycling stability, surpassing E140 at cycle12 and retaining a cycle100 capacity of 109 mAh g^{-1} that is 77% of the cycle2 capacity (Fig. 4c). However, E140 retains a cycle100 capacity of 38 mAh g^{-1}, being much lower than that of E160. The sharp contrast of cycling stability highlights the importance of crystallinity. Repetitive Na-ion (de)intercalation induces structural strain that could damage the crystal structure. A high crystallinity could minimize the damage and thus enhance the structural integrity during cycling. Fig. 4d shows the rate performance of the samples. E160 delivers reversible capacities of 132, 120, 102, 78, 60 and 43 mAh g^{-1} at 0.05, 0.1, 0.2, 0.5, 1 and 2 A g^{-1}, respectively. The capacity is fully recovered to 132 mAh g^{-1} when the rate is reduced back to 0.05 mA g^{-1}. Stable charge/discharge profiles of E160 were obtained at all rates (Fig. S2 in the ESI†). Small voltage drop can be seen at high rates, suggesting a small polarization when increasing the rate. In contrast, E140 delivers lower capacities at all the increased rates and fails at a rate higher than 1 A g^{-1}. The obtained cycling stability and rate capability are among the best for the Na-intercalation in MoS$_2$ in the applied voltage window.[34,42,43] Our results present two implications that could benefit future

material engineering for Na-storage. First, the expanded interlayer spacing and structural disorder could kinetically facilitate Na-ion intercalation and diffusion within the van der Waal gaps. Second, a high degree of crystallinity could sustain the structural strain upon Na-ion (de)intercalation and maintain the structural integrity in the prolonged cycles. Therefore, a balance between the two factors needs to be taken into consideration when designing electrodes in SIBs.
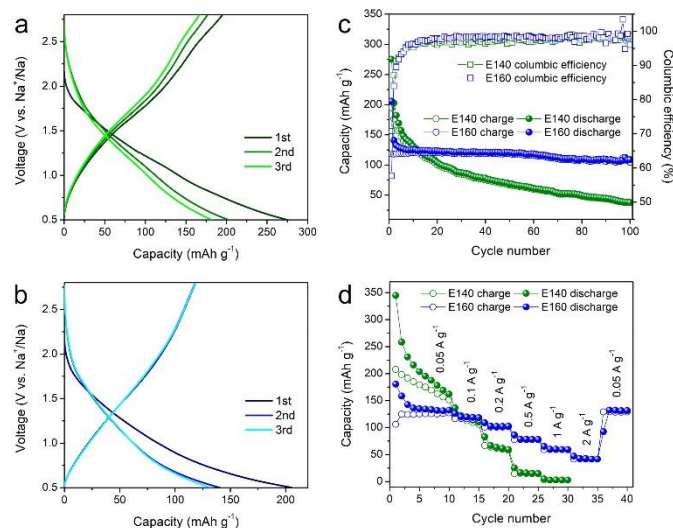

Fig. 4 Na-storage performance of E140 and E160. (a, b) Charge-discharge profiles of the first three cycles of E140 (a) and E160 (b) at 50 mA g^{-1}. (c) Comparison of cycling performance of E140 and E160 for 100 cycles at 50 mA g^{-1}. (d) Comparison of rate capability of E140 and E160 at a current density range of 0.05-2 A g^{-1}.

3.3 Kinetics study

Kinetics study was conducted to analyse the different electrochemical behaviour of the two samples and elucidate the facilitation of charge transfer/transport induced by expanding interlayer space. CV curves were recorded in a scan rate (v) range of 0.1-10 mV s^{-1}. As show in Fig. 5a and 5b, both current (i) increasing and peak voltage shifting are observed in the two samples when increasing the scan rate. E140 exhibits a significant shift of peak voltage as indicated by the arrow in Fig. 5a, resulting in severe distortion of the curves at high rates. In contrast, E160 exhibits a much smaller peak voltage shift (Fig. 5b) and thus a minimal distortion of the curves. The observed small change in voltage as a function of scan rate indicates a small polarization occurs in E160 upon fast Na-ion (de)intercalation, which agrees well with its better rate capability (Fig. 4f) and smaller separation between its charge and discharge curves at high rates (Fig. S2 in the ESI†) comparing with E140. According to the expression of $i = av^b$ where a and b are adjustable constants, and the b-value would be 0.5 for a semi-infinite linear diffusion-controlled process while close to 1.0 for a surface-controlled process.[44] As shown in Fig. S3 in the ESI†, the b-value of the desodiation (anodic scan) is determined to be 0.52 and 0.76 for E140 and E160, respectively. It indicates that the diffusional limitation in E140 is a graver issue than in

E160. The total discharge storage calculated from the CV curves is plotted as a function of discharge time in Fig. 5c. It indicates that the maximum value of E160, ~140 mAh g^{-1}, is in reasonable agreement with the value obtained from the galvanostatic discharging measurement. The decay trance of the discharge capacity shows a typical battery-type behaviour and suggests a diffusion dominated charge storage mechanism.[34,45-47] E160 exhibits a slower decay rate, which signals better Na-ion diffusion property. To further explore the ion diffusion property, discharge capacity is plotted as a function of $v^{-1/2}$. As shown in Fig. 5d, two distinct kinetic regions can be identified for each sample. For the case of E160, the discharge capacity decreases only gradually with the scan rate up to 1 mV s^{-1}, meaning that there is no obvious indication of diffusional limitation for a discharging time > 2300 s.[45,46] Above this scan rate, the discharge capacity decreases linearly, being agreement with the results in Fig. 5c. For the case of E140, diffusional limitation starts to govern the Na-storage at a scan rate of 0.2 mV s^{-1}, corresponding to the quick decrease at a discharging time < 11500 s in Fig. 5c. Based on the above analysis, E160 displays a better kinetic property of charge transfer/transport than E140, giving rise to its better cycling stability and rate capability.
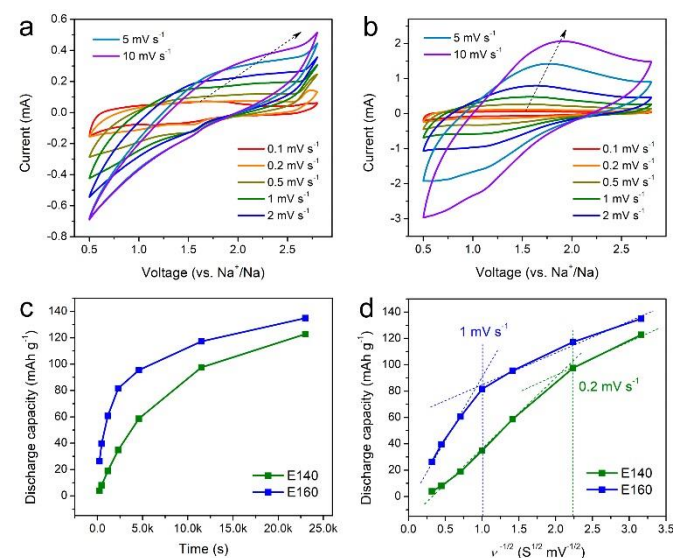

Fig. 5 Kinetics study of E140 and 160. (a, b) CV curves of E140 (a) and E160 (b) at a scan rate range of 0.1-10 mV s^{-1}. (c) Discharge capacity of E140 and E160 versus discharge time. As time → ∞ access to the diffusion limited redox sites can occur and so extension is estimated to be 140 mAh g^{-1}. (d) Discharge capacity of E140 and E160 versus the inverse square root of scan rate, showing different kinetic regions.

Electrochemical impedance spectroscopy was used to further analyse the charge transfer kinetics of the samples. The obtained Nyquist plots are shown in Fig. 6 and fitted using an equivalent circuit to extract resistance (Fig. S4 and Table 1 in the ESI†). As seen in Fig. 6a, the plot of E140 consists of two parts after the 2nd cycle. A small semicircle at high frequencies arises from the ionic transport through solid-electrolyte-interphase (SEI), and a quasi-semicircle and a Warburg tail at mid-to-low

frequencies are ascribed to the charge transfer process in the material.[48] Notably, the charge transfer kinetics becomes much more sluggish after the 10th and 30th cycle, as suggested by both the low frequency before reaching the maximum frequency and large diameter of the second semicircle.[49] Evidently, R_{ct} increases greatly from 53.9 Ω at the 2nd cycle to 4907 Ω at the 10th cycle. The severely deteriorated charge transfer kinetics is caused by the damaged structure of E140 after repeated (de)intercalation of Na-ions over cycles. In contrast, the plots of E160 (Fig. 6b) are characterized by different electrochemical features. Besides the small semicircle arising from SEI at high frequencies, much smaller charge transfer quasi-semicircles are shown at mid-to-low frequencies and are in part blended with the Warburg tail at low frequencies.[49] It suggests the charge transfer kinetics of E160 is much better comparing to E140, which is evidence by the small increase of R_{ct} from 101.8 Ω at the 2nd cycle to 295.3 Ω at the 30th cycle. Therefore, the EIS analysis once again demonstrates a better change transfer kinetic property of E160 owing to its expanded interlayer spacing and great structural stability.
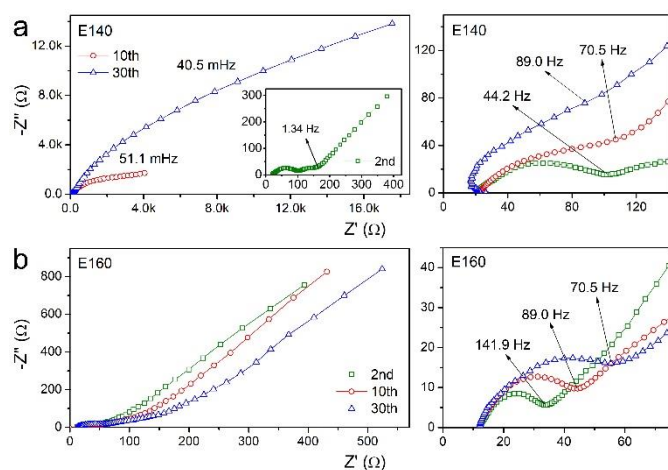

Fig. 6 EIS analysis of E140 (a) and E160 (b). The Nyquist plots are recorded after the 2nd, 10th and 30th cycle. The left column shows the plots in the full frequency region and the right column shows the magnified plots in the high-mid frequency region.

4. Conclusions

In summary, a substantial expansion of MoS$_2$ interlayer spacing to 1 nm is achieved by a facile hydrothermal route at low temperatures of 140 and 160°C. Used as SIB anodes, the MoS$_2$ nanosheets exhibit one of the best Na-storage performances in the applied voltage window of 0.5-2.8 V. Kinetics study verifies the facilitation of charge transfer/transport induced by the expanded interlayer spacing, which is evidenced by the alleviation of diffusional limitation. Our work presents a rational exploitation of the van der Waals gaps as 2D diffusion pathways to improve SIB performance, and the obtained results highlight the significance of utilizing materials' structural features for ion storage. We hope this work could offer valuable insights for researchers working with 2D TMDs or materials with other

prominent features in various energy storage and conversion systems.

Conflicts of interest

There are no conflicts to declare.

Acknowledgements

References

1   F. Bonaccorso, L. Colombo, G. Yu, M. Stoller, V. Tozzini, A. C. Ferrari, R. S. Ruoff and V. Pellegrini, *Science*, 2015, **347**, 1246501.
2   C. Tan, X. Cao, X.-J. Wu, Q. He, J. Yang, X. Zhang, J. Chen, W. Zhao, S. Han and G.-H. Nam, *Chem. Rev.*, 2017, **117**, 6225-6331.
3   Y. Sun, S. Gao, F. Lei and Y. Xie, *Chem. Soc. Rev.*, 2015, **44**, 623-636.
4   Y. Xu, M. Zhou, X. Wang, C. Wang, L. Liang, F. Grote, M. Wu, Y. Mi and Y. Lei, *Angew. Chem. Int. Ed.*, 2015, **54**, 8768-8771.
5   H. Zhu, C. Xiao, H. Cheng, F. Grote, X. Zhang, T. Yao, Z. Li, C. Wang, S. Wei, Y. Lei and Y. Xie, *Nature Commun.*, 2014, **5**, 3960.
6   Y. Mi, L. Wen, Z. Wang, D. Cao, Y. Fang and Y. Lei, *Appl. Catal. B*, 2015, **176-177**, 331-337.
7   S. Manzeli, D. Ovchinnikov, D. Pasquier, O. V. Yazyev and A. Kis, *Nat. Rev. Mater.*, 2017, **2**, 17033.
8   X. Chia, A. Y. S. Eng, A. Ambrosi, S. M. Tan and M. Pumera, *Chem. Rev.*, 2015, **115**, 11941-11966.
9   J. Xu, J. Zhang, W. Zhang and C. S. Lee, *Adv. Energy Mater.*, 2017.
10 T. Wang, S. Chen, H. Pang, H. Xue and Y. Yu, *Adv. Sci.*, 2017, **4**, 1600289.
11 G. Zhang, H. Liu, J. Qu and J. Li, *Energy Environ. Sci.*, 2016, **9**, 1190-1209.
12 Y. Cao, L. Xiao, M. L. Sushko, W. Wang, B. Schwenzer, J. Xiao, Z. Nie, L. V. Saraf, Z. Yang and J. Liu, *Nano Lett.*, 2012, **12**, 3783-3787.
13 Y. Wen, K. He, Y. Zhu, F. Han, Y. Xu, I. Matsuda, Y. Ishii, J. Cumings and C. Wang, *Nature Commun.*, 2014, **5**, 4033.
14 D. Su, S. Dou and G. Wang, *Adv. Energy Mater.*, 2015, **5**, 1401205.
15 M. Xu, F. Yi, Y. Niu, J. Xie, J. Hou, S. Liu, W. Hu, Y. Li and C. M. Li, *J. Mater. Chem. A*, 2015, **3**, 9932-9937.
16 T. S. Sahu and S. Mitra, *Sci. Rep.*, 2015, **5**, 12571.
17 Y. Lu, Q. Zhao, N. Zhang, K. Lei, F. Li and J. Chen, *Adv. Funct. Mater.*, 2016, **26**, 911-918.
18 R. Wang, S. Gao, K. Wang, M. Zhou, S. Cheng and K. Jiang, *Sci. Rep.* 2017, **7**, 7963.
19 Z.-T. Shi, W. Kang, J. Xu, Y.-W. Sun, M. Jiang, T.-W. Ng, H.-T. Xue, Y. Denis, W. Zhang and C.-S. Lee, *Nano Energy*, 2016, **22**, 27-37.
20 Y. Liu, X. Wang, X. Song, Y. Dong, L. Yang, L. Wang, D. Jia, Z. Zhao and J. Qiu, *Carbon*, 2016, **109**, 461-471.
21 H. Wang, H. Jiang, Y. Hu, N. Li, X. Zhao and C. Li, *J. Mater. Chem. A*, 2017, **5**, 5383-5389.
22 Z. Gao, X. Yu, J. Zhao, W. Zhao, R. Xu, Y. Liu and H. Shen, *Nanoscale*, 2017, **9**, 15558-15565.
23 X. Wang, Z. Guan, Y. Li, Z. Wang and L. Chen, *Nanoscale*, 2015, **7**, 637-641.

24 J. Wang, C. Luo, T. Gao, A. Langrock, A. C. Mignerey and C. Wang, *Small*, 2015, **11**, 473-481.

25 X. Fang, C. Hua, X. Guo, Y. Hu, Z. Wang, X. Gao, F. Wu, J. Wang and L. Chen, *Electrochim. Acta*, 2012, **81**, 155-160.

26 J. Xie, J. Zhang, S. Li, F. Grote, X. Zhang, H. Zhang, R. Wang, Y. Lei, B. Pan and Y. Xie, *J. Am. Chem. Soc.*, 2013, **135**, 17881-17888.

27 M. Chatti, T. Gengenbach, R. King, L. Spiccia and A. N. Simonov, *Chem. Mater.*, 2017, **29**, 3092-3099.

28 M. Acerce, D. Voiry and M. Chhowalla, *Nat. Nanotechnol.*, 2015, **10**, 313.

29 X. Xie, T. Makaryan, M. Zhao, K. L. Van Aken, Y. Gogotsi and G. Wang, *Adv. Energy Mater.*, 2016, **6**, 1502161.

30 X. Fan, R. R. Gaddam, N. A. Kumar and X. S. Zhao, *Adv. Energy Mater.*, 2017, **7**, 1700317.

31 Z. Xiang, Z. Zhang, X. Xu, Q. Zhang and C. Yuan, *Carbon*, 2016, **98**, 84-89.

32 J. Xie, H. Zhang, S. Li, R. Wang, X. Sun, M. Zhou, J. Zhou, X. W. D. Lou and Y. Xie, *Adv. Mater.*, 2013, **25**, 5807-5813.

33 S. Zhang, X. Yu, H. Yu, Y. Chen, P. Gao, C. Li and C. Zhu, *ACS Appl. Mater. Interfaces*, 2014, **6**, 21880-21885.

34 J. B. Cook, H. S. Kim, Y. Yan, J. S. Ko, S. Robbennolt, B. Dunn and S. H. Tolbert, *Adv. Energy Mater.*, 2016, **6**, 1501937.

35 J. Park, J.-S. Kim, J.-W. Park, T.-H. Nam, K.-W. Kim, J.-H. Ahn, G. Wang and H.-J. Ahn, *Electrochim. Acta*, 2013, **92**, 427-432.

36 X. Wang, X. Shen, Z. Wang, R. Yu and L. Chen, *ACS Nano*, 2014, **8**, 11394-11400.

37 H. Wang, D. Mitlin, J. Ding, Z. Li and K. Cui, *J. Mater. Chem. A*, 2016, **4**, 5149-5158.

38 M. Zhou, Y. Xu, C. Wang, Q. Li, J. Xiang, L. Liang, M. Wu, H. Zhao and Y. Lei, *Nano Energy*, 2017, **31**, 514-524.

39 M. Zhou, Y. Xu, J. Xiang, C. Wang, L. Liang, L. Wen, Y. Fang, Y. Mi and Y. Lei, *Adv. Energy Mater.*, 2016, **6**, 1600448.

40 Y. Xu, M. Zhou, C. Zhang, C. Wang, L. Liang, Y. Fang, M. Wu, L. Cheng and Y. Lei, *Nano energy*, 2017, **38**, 304-312.

41 L. Fan, X. Li, B. Yan, J. Feng, D. Xiong, D. Li, L. Gu, Y. Wen, S. Lawes and X. Sun, *Adv. Energy Mater.*, 2016, **6**, 1502057.

42 G. S. Bang, K. W. Nam, J. Y. Kim, J. Shin, J. W. Choi and S.-Y. Choi, *ACS Appl. Mater. Interfaces*, 2014, **6**, 7084-7089.

43 L. Huang, Q. Wei, X. Xu, C. Shi, X. Liu, L. Zhou and L. Mai, *Phys. Chem. Chem. Phys.*, 2017, **19**, 13696-13702.

44 V. Augustyn, J. Come, M. A. Lowe, J. W. Kim, P.-L. Taberna, S. H. Tolbert, H. D. Abruna, P. Simon and B. Dunn, *Nat. Mater.*, 2013, **12**, 518-522.

45 Z. Li, J. Ding, H. Wang, K. Cui, T. Stephenson, D. Karpuzov and D. Mitlin, *Nano Energy*, 2015, **15**, 369-378.

46 L. Wen, Z. Wang, Y. Mi, R. Xu, S. Yu and Y. Lei, *Small*, 2015, **11**, 3408-3428.

47 L. Liang, Y. Xu, Y. Lei and H. Liu, *Nanoscale*, 2014, **6**, 3536-3539.

48 D. Aurbach, *J. Power Sources*, 2000, **89**, 206-218.

49 W. Li, X. Liu, H. Celio, P. Smith, A. Dolocan, M. Chi and A. Manthiram, *Adv. Energy Mater.*, 2018, 1703154.